Proceedings of the
Annual Stability Conference
Structural Stability Research Council
Louisville, Kentucky, April 1-4, 2025

Nonlinear GBT for thin truncated conical shells with circular cross-section

Victor Dan Popa[1], Mihai Nedelcu [2], Rodrigo Gonçalves [3]

Abstract
The paper presents the first Generalized Beam Theory (GBT) formulation for second-order (geometrically nonlinear) analysis of isotropic thin truncated conical shells with circular cross-section. The GBT cross-section kinematics adopted can describe accurately the global and distortional/local deformation of conical shells, while allowing for the standard GBT assumptions, a particularly relevant feature for the overall performance of the formulation. A suitable geometrically non-linear GBT-based beam finite element is proposed and, even though the resulting expressions are quite involved due to the complex kinematics of conical shells, they are presented in a straightforward vector-matrix notation. To illustrate the capabilities of the proposed formulation and its finite element implementation, several numerical examples are presented and discussed. For comparison and validation purposes, refined shell finite element model results are presented. It is shown that the proposed finite element leads to extremely accurate results for first-order and buckling (linear stability) analyses, and is quite accurate for second-order analyses up to fairly large displacements, while providing an insightful modal solution, triggering a relatively small number of deformation modes and requiring only a few finite elements.

1. Introduction

Thin-walled conical shells are quite efficient from a structural point of view, which makes them widely utilized across various engineering fields, as pressure vessels, storage tanks and silos, rocket components, towers, chimneys and poles for supporting lighting and telecommunications equipment, among others. Their geometrically non-linear behavior is quite complex, namely due to their imperfection sensitivity, and therefore an accurate structural analysis requires computationally demanding refined shell finite element models. Although Generalized Beam Theory (GBT) — a thin-walled beam theory capable of capturing cross-section in-plane and out-of-plane deformation (Schardt, 1989) — has been recognized as an efficient alternative to shell and finite strip models, its development for conical shells is still in its early stages.

This paper presents the first geometrically nonlinear GBT formulation for truncated conical shells with circular cross-section. While previous formulations for the linear stability case (calculation of bifurcation loads and buckling modes discarding pre-buckling deflections) neglect certain

[1] PhD student, Technical University of Cluj-Napoca, Romania <Victor.Popa@mecon.utcluj.ro>
[2] Professor, Technical University of Cluj-Napoca, Romania <mihai.nedelcu@mecon.utcluj.ro>
[3] Full Professor, CERIS and Universidade Nova de Lisboa, Portugal <rodrigo.goncalves@fct.unl.pt>

membrane strain components (Nedelcu, 2011; Mureşan et al., 2019), very recently a new approach for the first-order case was proposed that considers all the (linear) membrane strains and satisfies exactly the standard GBT membrane strain assumptions (Gonçalves & Nedelcu, 2024), leading to a more comprehensive and accurate characterization of the shell kinematics. This enhanced formulation necessarily introduces a more complex definition of the boundary conditions and relations between deformation mode amplitude functions. However, it also facilitates a consistent (geometrically exact) definition of the so-called "Vlasov warping" deformation modes, which are crucial for achieving high accuracy and computational efficiency. In this paper this first-order approach is extended to the geometric nonlinear setting, including bifurcation (linear stability) and second-order path-following analyses.

The outline of the paper is as follows. Section 2 presents the fundamental relations pertaining to conical shells, namely the strain-displacement and stress-strain relations, as well as the equilibrium equations. Section 3 develops the previous equations according to the GBT concept and provides all required equations for implementing a suitable geometrically non-linear displacement-based finite element. Several numerical examples are presented in Section 4, to show the capabilities of the proposed GBT-based finite element. The paper closes in Section 5, which contains the concluding remarks.

For the notation, subscript commas represent derivatives (e.g., $f_{,y} = \partial f/\partial y$) while the prime symbol represents derivatives with respect to the meridional coordinate x (e.g., $f' = \partial f/\partial x$). Superscripts $(\cdot)^{M,L}$ and $(\cdot)^{B,L}$ refer to the linear membrane and bending components, while $(\cdot)^{M,NL}$ is used for nonlinear membrane components.

2. Fundamental relations

Consider the truncated conical shell with circular cross-section illustrated in Fig. 1. In the coordinate system (x, θ, z), where x represents the meridional direction and z is the through-thickness coordinate, with $z = 0$ corresponding to the mid-surface, the shell volume is defined by the following ranges: $x \in [0, L], \theta \in [0, 2\pi]$, and $z \in [-t/2, t/2]$, where L is the meridional length, and t is the shell thickness. The radius of the cross-section is described as $r(x) = r_0 + x \sin\alpha$, where r_0 is the initial radius, and α is the semi-vertex angle.

Using the mid-surface displacement components (u, v, w) shown in the figure, the linear and nonlinear parts of the Green-Lagrange membrane and bending strains, for very thin conical shells, are as follows (see e.g. Leissa, 1973 and Goldfeld, 2007)

$$E_{xx}^{M,L} = u', \quad E_{\theta\theta}^{M,L} = \frac{v_{,\theta} + wc + us}{r}, \quad 2E_{x\theta}^{M,L} = \frac{u_{,\theta} - vs}{r} + v', \tag{1}$$

$$E_{xx}^{B,L} = -zw'', \; E_{\theta\theta}^{B,L} = -z\left(\frac{w_{,\theta\theta} - v_{,\theta}c}{r^2} + \frac{w's}{r}\right), \; 2E_{x\theta}^{B,L} = -2z\left(\frac{w'_{,\theta} - v'c}{r} + \frac{vsc - w_{,\theta}s}{r^2}\right), \tag{2}$$

$$E_{xx}^{M,NL} = \frac{w'^2}{2} + \frac{v'^2}{2}, \; E_{\theta\theta}^{M,NL} = \frac{1}{2}\left(\frac{vc - w_{,\theta}}{r}\right)^2 + \frac{1}{2}\left(\frac{v_{,\theta} + wc}{r}\right)^2, \; 2E_{x\theta}^{M,NL} = \frac{w'w_{,\theta}}{r} - \frac{w'vc}{r}, \tag{3}$$

where $c = \cos\alpha$, $s = \sin\alpha$. Note that the nonlinear bending strains are discarded. The strains can be written in a Voigt-like notation as (bold letters denote vectors and matrices)

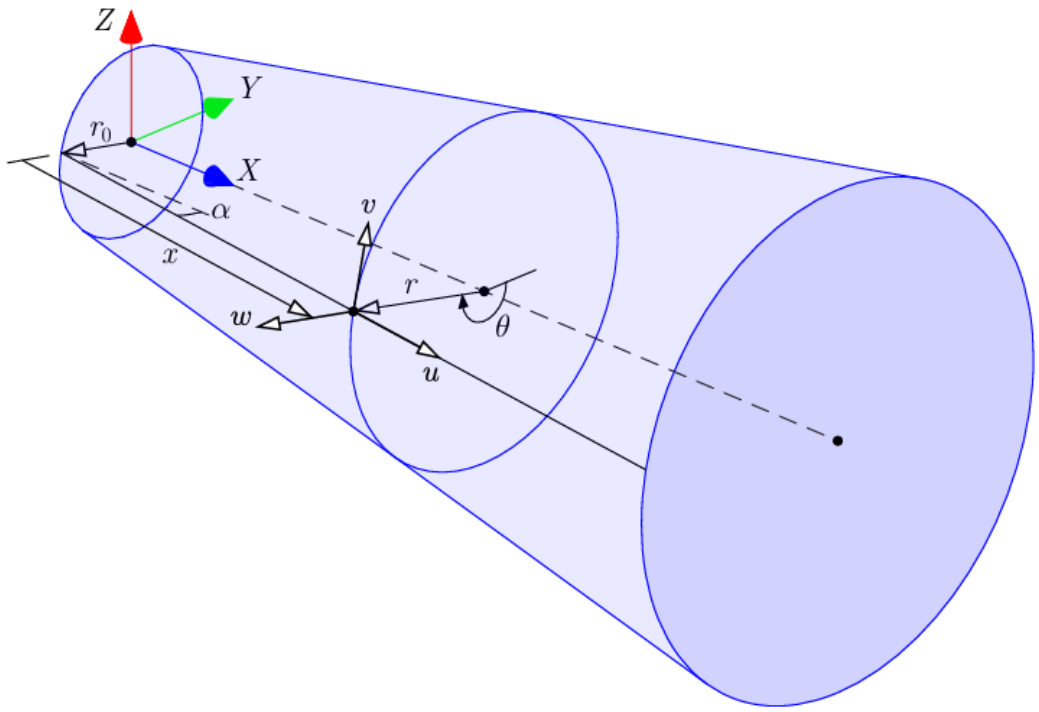

Figure 1: Truncated conical shell global/local axes and displacement components

$$\boldsymbol{E} = \begin{bmatrix} E_{xx} \\ E_{\theta\theta} \\ 2E_{x\theta} \end{bmatrix} = \boldsymbol{E}^{M,L} + \boldsymbol{E}^{B,L} + \boldsymbol{E}^{M,NL} = \begin{bmatrix} E_{xx}^{M,L} \\ E_{\theta\theta}^{M,L} \\ E_{x\theta}^{M,L} \end{bmatrix} + \begin{bmatrix} E_{xx}^{B,L} \\ E_{\theta\theta}^{B,L} \\ E_{x\theta}^{B,L} \end{bmatrix} + \begin{bmatrix} E_{xx}^{M,NL} \\ E_{\theta\theta}^{M,NL} \\ E_{x\theta}^{M,NL} \end{bmatrix}. \tag{4}$$

The stress state will be expressed using second Piola-Kirchoff stresses $\boldsymbol{S} = \boldsymbol{C}\boldsymbol{E}$, where $\boldsymbol{C}$ is the constitutive matrix, reading for a Saint Venant-Kirchoff material law

$$\boldsymbol{C} = \begin{bmatrix} \frac{E}{1-\mu^2} & \frac{\mu E}{1-\mu^2} & 0 \\ \frac{\mu E}{1-\mu^2} & \frac{E}{1-\mu^2} & 0 \\ 0 & 0 & G \end{bmatrix} = \begin{bmatrix} Q_{11} & Q_{12} & 0 \\ Q_{12} & Q_{11} & 0 \\ 0 & 0 & Q_{33} \end{bmatrix}, \tag{5}$$

with Young's modulus E, Poisson's ratio μ and shear modulus $G = E/2(1+\mu)$.

The equilibrium equations are obtained using the principle of virtual work. The internal part reads

$$\delta W_{int} = -\int_V \delta\boldsymbol{E}^T \boldsymbol{S}\, \mathrm{d}V = -\int_V \delta\boldsymbol{E}^T \boldsymbol{C}\boldsymbol{E}\, \mathrm{d}V\,, \tag{6}$$

and the external part, for mid-surface loads along local axes $\bar{\boldsymbol{q}}^T = [\bar{q}_x\ \bar{q}_\theta\ \bar{q}_z]$, is given by

$$\delta W_{ext} = \int_0^L \int_0^{2\pi} \delta\bar{\boldsymbol{U}}^T \bar{\boldsymbol{q}}\, r\, \mathrm{d}\theta\, \mathrm{d}x, \tag{7}$$

with the mid-surface displacement vector $\bar{\boldsymbol{U}} = [u\ v\ w]^T$.

3. The GBT approach for conical shells

A general formulation without further simplifications can be derived using separate approximations for each displacement component, following the standard procedure for conical shells (Leissa, 1973), leading to

$$u = \sum_{k=1}^{D} \bar{u}_k(\theta)\psi_k(x) = \bar{\boldsymbol{u}}^T\boldsymbol{\psi}, \tag{8}$$
$$v = \sum_{k=1}^{D} \bar{v}_i(\theta)\phi_i(x) = \bar{\boldsymbol{v}}^T\boldsymbol{\phi}, \tag{9}$$
$$w = \sum_{k=1}^{D} \bar{w}_j(\theta)\varphi_j(x) = \bar{\boldsymbol{w}}^T\boldsymbol{\varphi}, \tag{10}$$

where $(\bar{u}_k, \bar{v}_k, \bar{w}_k)$ are known functions — the so-called GBT "cross-section deformation modes" — and $(\psi_k, \phi_i, \varphi_j)$ are unknown mode amplitude functions. This allows writing the strain-displacement relations in a vector-matrix form as follows

$$\boldsymbol{E}^{M,L} = \boldsymbol{\Xi}_E^{M,L}\boldsymbol{\Phi}, \tag{11}$$
$$\boldsymbol{E}^{B,L} = z\boldsymbol{\Xi}_E^{B,L}\boldsymbol{\Phi}, \tag{12}$$
$$\boldsymbol{E}^{M,NL} = \boldsymbol{U}_1\boldsymbol{\Phi}^T\boldsymbol{\Xi}_{xx}^{M,NL}\boldsymbol{\Phi} + \boldsymbol{U}_2\boldsymbol{\Phi}^T\boldsymbol{\Xi}_{\theta\theta}^{M,NL}\boldsymbol{\Phi} + \boldsymbol{U}_3\boldsymbol{\Phi}^T\boldsymbol{\Xi}_{x\theta}^{M,NL}\boldsymbol{\Phi}, \tag{13}$$
$$\boldsymbol{\Phi}^T = [\boldsymbol{\psi}^T \quad (\boldsymbol{\psi}')^T \quad \boldsymbol{\phi}^T \quad (\boldsymbol{\phi}')^T \quad \boldsymbol{\varphi}^T \quad (\boldsymbol{\varphi}')^T \quad (\boldsymbol{\varphi}'')^T], \tag{14}$$

with the auxiliary matrices, obtained from Eqs. (1-3),

$$\boldsymbol{\Xi}_E^{M,L} = \begin{bmatrix} \mathbf{0} & \bar{\boldsymbol{u}}^T & \mathbf{0} & \mathbf{0} & \mathbf{0} & \mathbf{0} & \mathbf{0} \\ \frac{s\bar{\boldsymbol{u}}^T}{r} & \mathbf{0} & \frac{\bar{\boldsymbol{v}}_{,\theta}^T}{r} & \mathbf{0} & \frac{c\bar{\boldsymbol{w}}^T}{r} & \mathbf{0} & \mathbf{0} \\ \frac{\bar{\boldsymbol{u}}_{,\theta}^T}{r} & \mathbf{0} & \frac{-s\bar{\boldsymbol{v}}^T}{r} & \bar{\boldsymbol{v}}^T & \mathbf{0} & \mathbf{0} & \mathbf{0} \end{bmatrix} \tag{15}$$

$$\boldsymbol{\Xi}_E^{B,L} = -\begin{bmatrix} \mathbf{0} & \mathbf{0} & \mathbf{0} & \mathbf{0} & \mathbf{0} & \mathbf{0} & \bar{\boldsymbol{w}}^T \\ \mathbf{0} & \mathbf{0} & \frac{-c\bar{\boldsymbol{v}}_{,\theta}^T}{r^2} & \mathbf{0} & \frac{\bar{\boldsymbol{w}}_{,\theta\theta}^T}{r^2} & \frac{s\bar{\boldsymbol{w}}^T}{r} & \mathbf{0} \\ \mathbf{0} & \mathbf{0} & \frac{2sc\bar{\boldsymbol{v}}^T}{r^2} & \frac{-2c\bar{\boldsymbol{v}}^T}{r} & \frac{-2s\bar{\boldsymbol{w}}_{,\theta}^T}{r^2} & \frac{2\bar{\boldsymbol{w}}_{,\theta}^T}{r} & \mathbf{0} \end{bmatrix} \tag{16}$$

$$\boldsymbol{\Xi}_{xx}^{M,NL} = \frac{1}{2}\boldsymbol{\Xi}_A^T\boldsymbol{\Xi}_A, \quad \boldsymbol{\Xi}_{\theta\theta}^{M,NL} = \frac{1}{2r^2}\boldsymbol{\Xi}_B^T\boldsymbol{\Xi}_B, \quad \boldsymbol{\Xi}_{x\theta}^{M,NL} = \frac{1}{r}\boldsymbol{\Xi}_C^T\boldsymbol{\Xi}_D, \tag{17}$$

where $\boldsymbol{U}_1 = [1\ 0\ 0]^T$, $\boldsymbol{U}_2 = [0\ 1\ 0]^T$, $\boldsymbol{U}_3 = [0\ 1\ 0]^T$ are used to place the nonlinear components in the correct row and the following matrices are used to construct the *NL* components

$$\boldsymbol{\Xi}_A = \begin{bmatrix} \mathbf{0}\ \mathbf{0}\ \mathbf{0}\ \bar{\boldsymbol{v}}\ \mathbf{0}\ \mathbf{0}\ \mathbf{0}\ \mathbf{0}\ \mathbf{0}\ \bar{\boldsymbol{v}} \\ \mathbf{0}\ \mathbf{0}\ \mathbf{0}\ \mathbf{0}\ \mathbf{0}\ \bar{\boldsymbol{w}}\ \mathbf{0}\ \mathbf{0}\ \mathbf{0}\ \mathbf{0} \end{bmatrix}, \quad \boldsymbol{\Xi}_B = \begin{bmatrix} \mathbf{0}\ \mathbf{0}\ \bar{\boldsymbol{v}}c\ \mathbf{0}\ -\bar{\boldsymbol{w}}_{,\theta}\ \mathbf{0}\ \mathbf{0}\ \mathbf{0}\ \bar{\boldsymbol{v}}c\ \mathbf{0} \\ \mathbf{0}\ \mathbf{0}\ \bar{\boldsymbol{v}}_{,\theta}\ \mathbf{0}\ \bar{\boldsymbol{w}}c\ \mathbf{0}\ \mathbf{0}\ \mathbf{0}\ \bar{\boldsymbol{v}}_{,\theta}\ \mathbf{0} \end{bmatrix}, \tag{18}$$

$$\boldsymbol{\Xi}_C = \begin{bmatrix} \mathbf{0}\ \mathbf{0}\ \mathbf{0}\ \mathbf{0}\ \mathbf{0}\ \bar{\boldsymbol{w}}\ \mathbf{0}\ \mathbf{0}\ \mathbf{0}\ \mathbf{0}\ \mathbf{0} \\ \mathbf{0}\ \mathbf{0}\ -\bar{\boldsymbol{v}}\ \mathbf{0}\ \mathbf{0}\ \mathbf{0}\ \mathbf{0}\ \mathbf{0}\ -\bar{\boldsymbol{v}}\ \mathbf{0} \end{bmatrix}, \quad \boldsymbol{\Xi}_D = \begin{bmatrix} \mathbf{0}\ \mathbf{0}\ \mathbf{0}\ \mathbf{0}\ \bar{\boldsymbol{w}}_{,\theta}\ \mathbf{0}\ \mathbf{0}\ \mathbf{0}\ \mathbf{0}\ \mathbf{0}\ \mathbf{0} \\ \mathbf{0}\ \mathbf{0}\ \mathbf{0}\ \mathbf{0}\ \mathbf{0}\ \bar{\boldsymbol{w}}c\ \mathbf{0}\ \mathbf{0}\ \mathbf{0}\ \mathbf{0}\ \mathbf{0} \end{bmatrix}. \tag{19}$$

To construct the standard GBT Vlasov shell-type deformation modes, which satisfy $\varepsilon_{\theta\theta}^M = \gamma_{x\theta}^M = 0$ exactly for small displacements, the cross-section displacement components for the deformation mode *k* are defined using the basis functions

$$\omega_{2m} = \sin m\theta\,, \omega_{2m+1} = \cos m\theta\,, \tag{20}$$

where m is the number of circumferential waves. The Vlasov modes are as follows

$$\bar{u}_k = \omega_k,\ \ \bar{v}_k = -\omega_{k,\theta},\ \ \bar{w}_k = -\frac{\omega_k}{c}. \tag{21}$$

The Vlasov ($\gamma_{x\theta}^M = 0$) and null membrane transverse extension ($\varepsilon_{\theta\theta}^M = 0$) assumptions lead to the following relations between the modal amplitude functions

$$\psi_k = -s\phi_k + r\phi_k',\quad \varphi_k = (m^2 - s^2)\phi_k + sr\phi_k'. \tag{22}$$

To allow for non-null membrane shear strains and transverse extensions, if required, the Vlasov modes are supplemented by two sets of deformation modes *i* and *j*, using the same basis functions,

$$u = \sum_{i=1}^{D} \bar{u}_i\psi_i,\quad \bar{u}_i = \omega_i,\quad \bar{v}_i = \bar{w}_i = 0, \tag{23}$$

$$v = \sum_{j=1}^{D} \bar{v}_j\phi_j,\quad \bar{v}_1 = 1,\quad \bar{v}_{j>1} = -\omega_{j,\theta},\ \bar{u}_j = \bar{w}_j = 0. \tag{24}$$

The axial extension mode corresponds to i = 1 and the torsion mode corresponds to j = 1. The axisymmetric (indicated by the subscript *as*) mode is introduced separately by considering $\bar{w}_{as} = 1, \bar{u}_{as} = \bar{v}_{as} = 0$.

The virtual variation of the Green-Lagrange strain tensor becomes

$$\delta\boldsymbol{E} = \underbrace{\left(\boldsymbol{\Xi}_E^{B,L} + \boldsymbol{\Xi}_E^{M,L} + 2\boldsymbol{U}_1\boldsymbol{\Phi}^T\boldsymbol{\Xi}_{xx}^{M,NL} + 2\boldsymbol{U}_2\boldsymbol{\Phi}^T\boldsymbol{\Xi}_{\theta\theta}^{M,NL} + \boldsymbol{U}_3\boldsymbol{\Phi}^T\left(\boldsymbol{\Xi}_{x\theta}^{M,NL} + \left(\boldsymbol{\Xi}_{x\theta}^{M,NL}\right)^T\right)\right)}_{\boldsymbol{\Xi}_{\delta E}}\delta\boldsymbol{\Phi}. \tag{25}$$

Introducing this expression into Eq. (6) and using Eqs. (11)-(13), one obtains

$$\delta W_{int} = -\int_V\ \delta\boldsymbol{\Phi}^T\boldsymbol{\Xi}_{\delta E}^T\boldsymbol{C}\big(\boldsymbol{\Xi}_E^B + \boldsymbol{\Xi}_E^{M,L} + \boldsymbol{U}_1\boldsymbol{\Phi}^T\boldsymbol{\Xi}_{xx}^{M,NL} + \boldsymbol{U}_2\boldsymbol{\Phi}^T\boldsymbol{\Xi}_{\theta\theta}^{M,NL} + \boldsymbol{U}_3\boldsymbol{\Phi}^T\boldsymbol{\Xi}_{x\theta}^{M,NL}\big)\boldsymbol{\Phi}r\ \mathrm{d}x\ \mathrm{d}\theta\ \mathrm{d}z. \tag{26}$$

The external part, from Eq. (7), becomes

$$\delta W_{ext} = \int_0^L\int_0^{2\pi}\delta\boldsymbol{\Phi}^T\boldsymbol{\Xi}_{\bar{U}}^T\bar{\boldsymbol{q}}\ r\,d\theta\,dx, \tag{27}$$

with

$$\bar{\boldsymbol{U}} = \boldsymbol{\Xi}_{\bar{U}}\boldsymbol{\Phi},\qquad \boldsymbol{\Xi}_{\bar{U}} = \begin{bmatrix} \bar{\boldsymbol{u}}^T & \boldsymbol{0} & \boldsymbol{0} & \boldsymbol{0} & \boldsymbol{0} & \boldsymbol{0} & \boldsymbol{0} \\ \boldsymbol{0} & \boldsymbol{0} & \bar{\boldsymbol{v}}^T & \boldsymbol{0} & \boldsymbol{0} & \boldsymbol{0} & \boldsymbol{0} \\ \boldsymbol{0} & \boldsymbol{0} & \boldsymbol{0} & \boldsymbol{0} & \bar{\boldsymbol{w}}^T & \boldsymbol{0} & \boldsymbol{0} \end{bmatrix}. \tag{28}$$

The finite element is obtained by approximating the amplitude functions in vector $\boldsymbol{\Phi}$ using quintic Hermite polynomials, since a clamped boundary condition requires setting $\phi_k'' = 0$. The interpolation for a single element can be written as

$$\boldsymbol{\Phi} = \boldsymbol{f}\boldsymbol{d}_e, \tag{29}$$

where $\boldsymbol{f}$ contains the interpolation functions together with the relations between the Vlasov amplitude functions ($\psi_k, \phi_k, \varphi_k$), given in Eq. (22) and vector $\boldsymbol{d}_e$ collects the degrees of freedom.

The element internal force vector can be written as

$$(\boldsymbol{F}_{int})_e = \boldsymbol{K}_{Se}\boldsymbol{d}_e,$$

where $\boldsymbol{K}_S$ stands for the secant stiffness matrix, which has three components depending on the coupling between the linear and nonlinear strain components,

$$(\boldsymbol{K}_S)_e = \boldsymbol{K}_L + \boldsymbol{K}_S^{L.NL} + \boldsymbol{K}_S^{NL.NL}, \tag{30}$$

where indices *L* represent the linear part and *L.NL* represent linear with non-linear couplings, while *NL.NL* represent non-linear with non-linear couplings. The linear stiffness matrix can be written as

$$\boldsymbol{K}_L = \int_V \boldsymbol{f}^T \left(\left(\boldsymbol{\Xi}_E^{B,L}\right)^T + \left(\boldsymbol{\Xi}_E^{M,L}\right)^T \right) \boldsymbol{C} \left(\boldsymbol{\Xi}_E^{B} + \boldsymbol{\Xi}_E^{M,L}\right) \boldsymbol{f} r \, \mathrm{d}x \, \mathrm{d}\theta \, \mathrm{d}z. \tag{31}$$

The linear with non-linear combinations stiffness matrix will be

$$\boldsymbol{K}_S^{L.NL} = t\left(\boldsymbol{K}_S^{L.NL.xx} + \boldsymbol{K}_S^{L.NL.\theta\theta} + \boldsymbol{K}_S^{L.NL.x\theta}\right), \tag{32}$$

with

$$\boldsymbol{K}_S^{L.NL.xx} = \int \oint (\boldsymbol{P}_{Lxx}\boldsymbol{d}_e^T\boldsymbol{P}_{NLxx} + 2\boldsymbol{P}_{NLxx}^T\boldsymbol{d}_e\boldsymbol{P}_{Lxx}^T) r \, \mathrm{d}x \, \mathrm{d}\theta, \tag{33}$$

$$\boldsymbol{K}_S^{L.NL.\theta\theta} = \int \oint \left(\boldsymbol{P}_{L\theta\theta}\boldsymbol{d}_e^T\boldsymbol{P}_{NL\theta\theta} + 2\boldsymbol{P}_{NL\theta\theta}^T\boldsymbol{d}_e\boldsymbol{P}_{L\theta\theta}^T\right) r \, \mathrm{d}x \, \mathrm{d}\theta, \tag{34}$$

$$\boldsymbol{K}_S^{L.NL.x\theta} = \int \oint \left(\boldsymbol{P}_{Lx\theta}\boldsymbol{d}_e^T\boldsymbol{P}_{NLx\theta 1} + \boldsymbol{P}_{NLx\theta 2}^T\boldsymbol{d}_e\boldsymbol{P}_{Lx\theta}^T\right) r \, \mathrm{d}x \, \mathrm{d}\theta, \tag{35}$$

and

$$\boldsymbol{P}_{Lxx} = \boldsymbol{f}^T\left(\boldsymbol{\Xi}_E^{M,L}\right)^T\boldsymbol{C}\boldsymbol{U}_1, \quad \boldsymbol{P}_{NLxx} = \boldsymbol{f}^T\boldsymbol{\Xi}_{xx}^{M,NL}\boldsymbol{f}, \tag{36}$$

$$\boldsymbol{P}_{L\theta\theta} = \boldsymbol{f}^T\left(\boldsymbol{\Xi}_E^{M,L}\right)^T\boldsymbol{C}\boldsymbol{U}_2, \quad \boldsymbol{P}_{NL\theta\theta} = \boldsymbol{f}^T\boldsymbol{\Xi}_{\theta\theta}^{M,NL}\boldsymbol{f}, \tag{37}$$

$$\boldsymbol{P}_{Lx\theta} = \boldsymbol{f}^T\left(\boldsymbol{\Xi}_E^{M,L}\right)^T\boldsymbol{C}\boldsymbol{U}_3 \quad \boldsymbol{P}_{NLx\theta 1} = \boldsymbol{f}^T\boldsymbol{\Xi}_{x\theta}^{M,NL}\boldsymbol{f} \quad \boldsymbol{P}_{NLx\theta 2} = \boldsymbol{f}^T\left(\boldsymbol{\Xi}_{x\theta}^{M,NL} + \left(\boldsymbol{\Xi}_{x\theta}^{M,NL}\right)^T\right)\boldsymbol{f}. \tag{38}$$

The non-linear with non-linear combinations stiffness matrix will be

$$\boldsymbol{K}_S^{NL.NL} = t\left(\boldsymbol{K}_S^{NL.NL.xx.xx} + \boldsymbol{K}_S^{NL.NL.\theta\theta.\theta\theta} + \boldsymbol{K}_S^{NL.NL.xx.\theta\theta} + \boldsymbol{K}_S^{NL.NL.x\theta.x\theta}\right), \tag{39}$$

with

$$\boldsymbol{K}_S^{NL.NL.xx.xx} = 2Q_{11}\int\oint \boldsymbol{P}_{NLxx}^T \boldsymbol{D}\boldsymbol{P}_{NLxx} r\,\mathrm{d}x\,\mathrm{d}\theta, \tag{40}$$

$$\boldsymbol{K}_S^{NL.NL.\theta\theta.\theta\theta} = 2Q_{22}\int\oint \boldsymbol{P}_{NL\theta\theta}^T \boldsymbol{D}\boldsymbol{P}_{NL\theta\theta} r\,\mathrm{d}x\,\mathrm{d}\theta, \tag{41}$$

$$\boldsymbol{K}_S^{NL.NL.xx.\theta\theta} = 2Q_{12}\int\oint \left(\boldsymbol{P}_{NLxx}^T \boldsymbol{D}\boldsymbol{P}_{NL\theta\theta} + \boldsymbol{P}_{NL\theta\theta}^T \boldsymbol{D}\boldsymbol{P}_{NLxx}\right) r\,\mathrm{d}x\,\mathrm{d}\theta, \tag{42}$$

$$\boldsymbol{K}_S^{NL.NL.x\theta.x\theta} = Q_{33}\int\oint \boldsymbol{P}_{NLx\theta 2}^T \boldsymbol{D}\boldsymbol{P}_{NLx\theta 1} r\,\mathrm{d}x\,\mathrm{d}\theta, \tag{43}$$

where $\boldsymbol{D} = \boldsymbol{d}_e \boldsymbol{d}_e^T$.

The element tangent stiffness matrix, which is required to perform Newton-Raphson iterations, has a similar form,

$$(\boldsymbol{K}_T)_e = \boldsymbol{K}_L + \boldsymbol{K}_T^{L.NL} + \boldsymbol{K}_T^{NL.NL}, \tag{44}$$

with

$$\boldsymbol{K}_T^{L.NL} = t\left(\boldsymbol{K}_T^{L.NL.xx} + \boldsymbol{K}_T^{L.NL.\theta\theta} + \boldsymbol{K}_T^{L.NL.x\theta}\right), \tag{45}$$

$$\boldsymbol{K}_T^{L.NL.xx} = \int\oint \left(\boldsymbol{P}_{Lxx}\boldsymbol{d}_e^T \boldsymbol{P}_{NLxx}^T + 2\boldsymbol{P}_{NLxx}^T (\boldsymbol{d}_e^T \boldsymbol{P}_{Lxx})\right) r\,\mathrm{d}x\,\mathrm{d}\theta, \tag{46}$$

$$\boldsymbol{K}_T^{L.NL.\theta\theta} = \int\oint \left(\boldsymbol{P}_{L\theta\theta}\boldsymbol{d}_e^T \boldsymbol{P}_{NL\theta\theta}^T + 2\boldsymbol{P}_{NL\theta\theta}^T (\boldsymbol{d}_e^T \boldsymbol{P}_{L\theta\theta})\right) r\,\mathrm{d}x\,\mathrm{d}\theta, \tag{47}$$

$$\boldsymbol{K}_T^{L.NL.x\theta} = \int\oint \left(\boldsymbol{P}_{Lx\theta}\boldsymbol{d}_e^T \boldsymbol{P}_{NLx\theta 1}^T + 2\boldsymbol{P}_{NLx\theta 2}^T (\boldsymbol{d}_e^T \boldsymbol{P}_{Lx\theta})\right) r\,\mathrm{d}x\,\mathrm{d}\theta, \tag{48}$$

$$\boldsymbol{K}_T^{NL.NL} = t\left(\boldsymbol{K}_T^{NL.NL.xx.xx} + \boldsymbol{K}_T^{NL.NL.\theta\theta.\theta\theta} + \boldsymbol{K}_T^{NL.NL.xx.\theta\theta} + \boldsymbol{K}_T^{NL.NL.x\theta.x\theta}\right), \tag{49}$$

$$\boldsymbol{K}_T^{NL.NL.xx.xx} = 2Q_{11}\int\oint \left(\boldsymbol{P}_{NLxx}^T \boldsymbol{D}\boldsymbol{P}_{NLxx}^T + \boldsymbol{P}_{NLxx}{}^T (\boldsymbol{d}_e^T \boldsymbol{P}_{NLxx}\boldsymbol{d}_e)\right) r\,\mathrm{d}x\,\mathrm{d}\theta, \tag{50}$$

$$\boldsymbol{K}_T^{NL.NL.\theta\theta.\theta\theta} = 2Q_{22}\int\oint \left(\boldsymbol{P}_{NL\theta\theta}^T \boldsymbol{D}\boldsymbol{P}_{NL\theta\theta}^T + \boldsymbol{P}_{NL\theta\theta}{}^T \left(\boldsymbol{d}_e{}^T \boldsymbol{P}_{NL\theta\theta}\boldsymbol{d}_e\right)\right) r\,\mathrm{d}x\,\mathrm{d}\theta, \tag{51}$$

$$\boldsymbol{K}_T^{NL.NL.xx.\theta\theta} = 2Q_{12}\int\oint \left(\boldsymbol{P}_{NL\theta\theta}^T \boldsymbol{D}\boldsymbol{P}_{NL\theta\theta}^T + \boldsymbol{P}_{NLxx}^T \left(\boldsymbol{d}_e{}^T \boldsymbol{P}_{NL\theta\theta}\boldsymbol{d}_e\right) + \boldsymbol{P}_{NL\theta\theta}^T \boldsymbol{D}\boldsymbol{P}_{NLxx}{}^T + \boldsymbol{P}_{NL\theta\theta}^T \left(\boldsymbol{d}_e{}^T \boldsymbol{P}_{NL\theta\theta}\boldsymbol{d}_e\right)\right) r\,\mathrm{d}x\,\mathrm{d}\theta, \tag{52}$$

$$\boldsymbol{K}_T^{NL.NL.x\theta.x\theta} = Q_{33}\int\oint \left(\boldsymbol{P}_{NLx\theta 2}^T \boldsymbol{D}\boldsymbol{P}_{NLx\theta 1}^T + \boldsymbol{P}_{NLx\theta 2}^T \left(\boldsymbol{d}_e{}^T \boldsymbol{P}_{NLx\theta 1}\boldsymbol{d}_e\right)\right) r\,\mathrm{d}x\,\mathrm{d}\theta. \tag{53}$$

The stiffness matrices are obtained by performing numerical integration using 6 Gauss points along *x*, which suffices to mitigate locking effects. Since for deformation modes with many waves, the numerical integration with respect to θ requires a high number of Gauss points, which can be computationally expensive, the integration was performed analytically. This process is challenging for the nonlinear stiffness matrices due to their dependence of the degrees of freedom vector $\boldsymbol{d}_e$, which changes at each iteration. In the present formulation each element of $\boldsymbol{d}_e$ (and $\boldsymbol{D}$) is multiplied with an influence matrix, different for each nonlinear stiffness matrix. These influence matrices are calculated by analytical integration along θ, before the starting of the Newton-Raphson iterative process.

The boundary conditions require special constraints between the degrees of freedom related with the supports, which are presented in detail in (Gonçalves & Nedelcu, 2024).

The finite element analysis was written in MATLAB (MathWorks Inc., 2024), together with post-processing scripts to enable the visualization of deformed configurations and buckling modes.

4. Numerical examples

To provide evidence of the potential of the proposed formulation, several numerical examples are presented next. The results are compared with shell finite element analysis (SFEA) results conducted in ADINA (Bathe, 2019) and ABAQUS (Hibbit et al., 2002), using MITC4 and S4 shell elements, respectively. The number of shell finite elements are set after sensitivity studies revealed the best discretizations. In all the presented cases the shell is made of steel, with E = 210000 MPa and μ=0.3.

4.1 Shell subjected to a distortional-type load

A shell with the following geometric setting is considered: top radius (X = 0) r_1 = 100 mm, semi-vertex angle α = 45°, meridian length L = 3000 mm, thickness t = 1 mm. The top end is simply supported (u = v = w = 0) and the other end is free. A distortional-type distributed load is applied at the end section, along the local z axis, triggering the m = 2 distortional deformation mode pair. The GBT model involves 30 finite elements, whereas the shell model involves approximately 9600 shell elements.

A linear (first-order) analysis is carried out and the results are shown in Fig. 2. An excellent agreement between the GBT and shell model deformed configurations is observed, with a negligible error in terms of the maximum displacement along Y. The predominant GBT deformation mode is the k = 5 Vlasov distortional mode, with a small end effect from the i = 5 shear mode.

A geometrically non-linear analysis was also performed, and the results are shown in Fig. 3. The shell results reveal a complex snap-back behaviour at a load factor of 0.102. Until this point the GBT and the shell nonlinear curves virtually overlap, showing that the proposed GBT formulation is capable of providing very accurate solutions for small to moderate displacements. Since only load control was implemented, without branch switching techniques, the GBT analysis is not able to detect the snap-back path and follows the initial path.

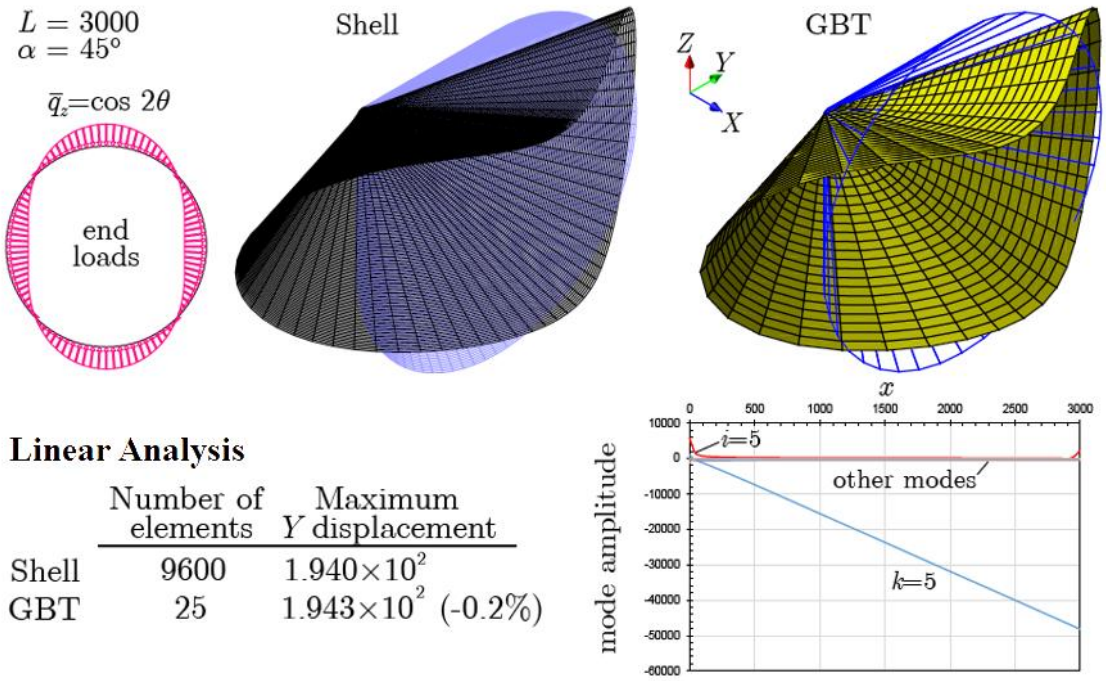

Linear Analysis

	Number of elements	Maximum Y displacement
Shell	9600	1.940×10^{2}
GBT	25	1.943×10^{2} (-0.2%)

Figure 2: Linear analysis of a shell subjected to a distortional-type (m = 2) distributed load

For the load factor of 0.102 the predominant deformation mode remains the k = 5 Vlasov mode, but the axisymmetric mode also plays an important role, together with the k = 9 Vlasov mode. The i, j = 5 modes have substantial contributions in representing the end effects.

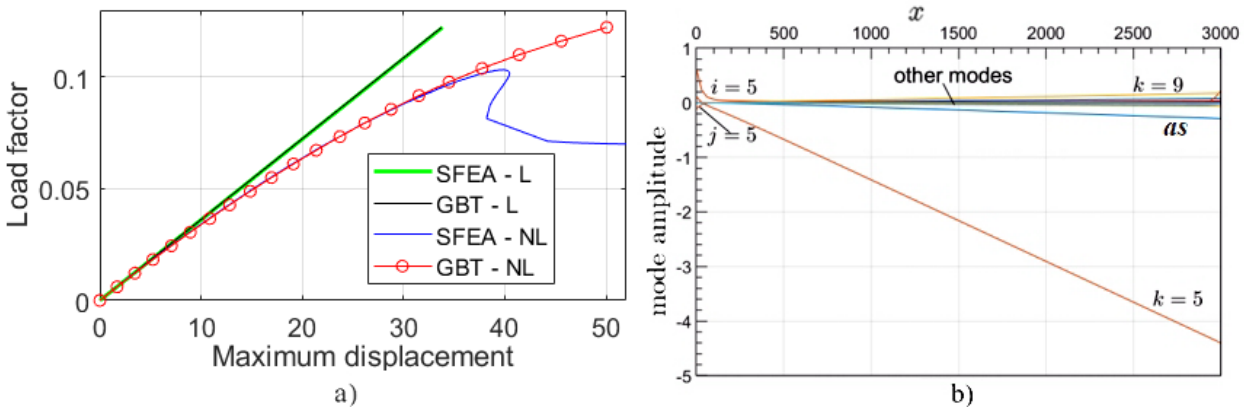

Figure 3: Geometrically non-linear analysis of a shell subjected to a distortional-type (m = 2) distributed load: a) equilibrium paths; b) mode amplitudes for the load factor of 0.102

4.2 Shell subjected to concentrated loads

For the linear (first-order) analysis the shell has the same geometry as in the previous example, except the length is changed to L = 1000 mm. The shell is subjected to a concentrated radial load (in Z direction) causing severe local deformations. Due to the increased complexity of the problem the analysis is carried out with 363 modes, because modes with a large number of circumferential waves are required to accurately represent the concentrated deformation near the load application

point. Nevertheless, there is only a dozen of modes with significant contributions. The mode amplitude graph makes it possible to identify several relevant modes: eight Vlasov (k = 2, 5, 6, 9, 10, 13, 14, 17), the modes i, j = 2 now play a global role and the end effects involve many modes, particularly i = 5, 6.

For the geometrically nonlinear analysis the thickness was modified to t = 2 mm, and the length is set to L = 3000 mm. The load was reversed to produce compression, thus making the model more flexible. The number of GBT modes is 303, and the number of finite elements is 20. The deformed configurations and the mode amplitude graph pertain to a load factor equal to 1. As seen from the equilibrium paths in Fig. 5, the GBT model is very accurate up to a maximum displacement of 83 mm, which corresponds to fairly large displacements (approximately 40 times the thickness), and afterwards becomes stiffer than the shell one. The mode amplitude graph reveals major contributions of modes k, i = 3, 5, 7, 9, 11, the axisymmetric mode, and j = 3 as end effects.

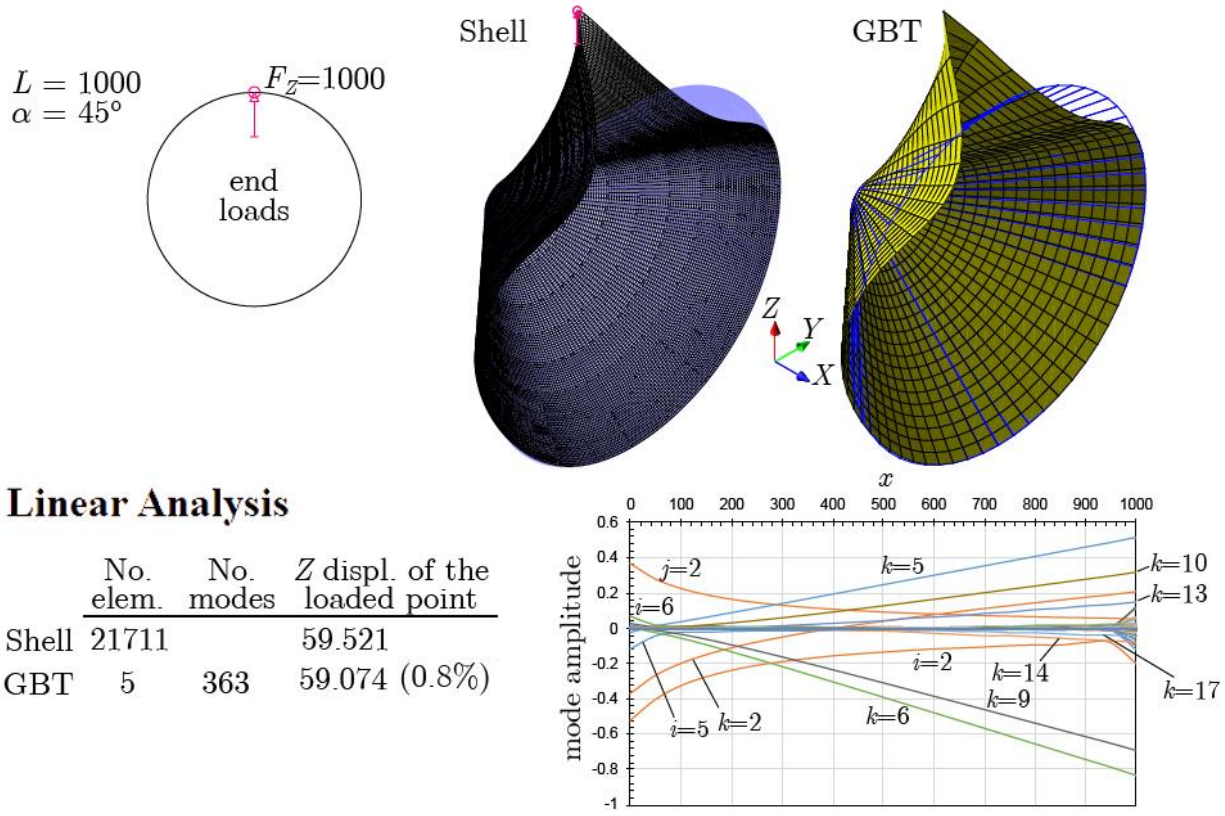

Figure 4: Linear analysis of a wide shell subjected to a radial load

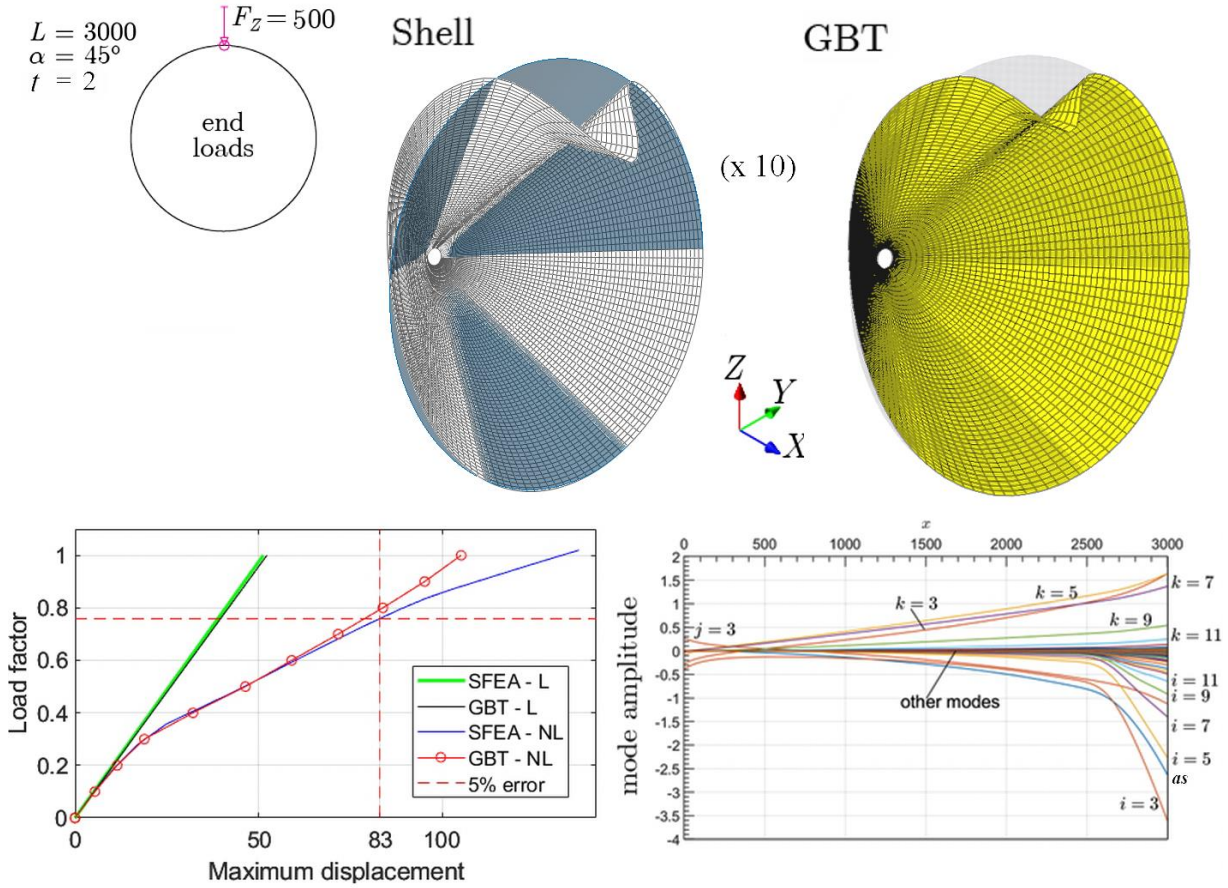

Figure 5: Geometrically nonlinear analysis of a wide shell subjected to a radial load (the deformed configurations and mode amplitude graph correspond to a load factor equal to 1)

4.3 Linear buckling of cantilever shells under axial compression

For the last example the thickness is set to t = 1 mm and the shell length is L_X = 1200 mm (length along X). The top radius is r_1= 50 mm, while the bottom radius r_2 varies between 50 mm and 1000 mm. These conical shells are analysed under an axial compressive force of P_0 = 1 kN. The end $X = L$ is clamped and the $X = 0$ end is free for all displacements and rotations. The number of GBT finite elements varies from 20 to 40 depending on radius size. For the shell models, the average size of the S4 finite elements is 5 mm, and their numbers greatly varies from 15120, for the cylinder, up to 205920, for the conical shell with the largest radius.

To obtain the bifurcation loads and corresponding buckling modes, a very small load step is carried out, to obtain the pre-buckling stresses, and the eigenvalue problem $[\boldsymbol{K}_L + \lambda(\boldsymbol{K}_T^{L.NL} + \boldsymbol{K}_T^{NL.NL})]\boldsymbol{d} = \boldsymbol{0}$ is solved (see Eq. (44)). Fig. 6 and Table 1 present the results in terms of critical buckling factors (λ_c) and mode shapes, which are in excellent agreement with the shell model results, having a percentage relative difference below 1%. For this special case of pure axial compression, there is no coupling between the GBT modes having different numbers of circumferential waves (m). Therefore, the critical shapes are represented by a single Vlasov mode (k) coupled with the corresponding shear and transverse extension modes (i, j) — no such insight is possible with shell finite element models. The mode amplitude graph given in Fig.7, shows that

for every case there is one dominant Vlasov mode but its *i* and *j* mode counterparts have non-negligible contributions .

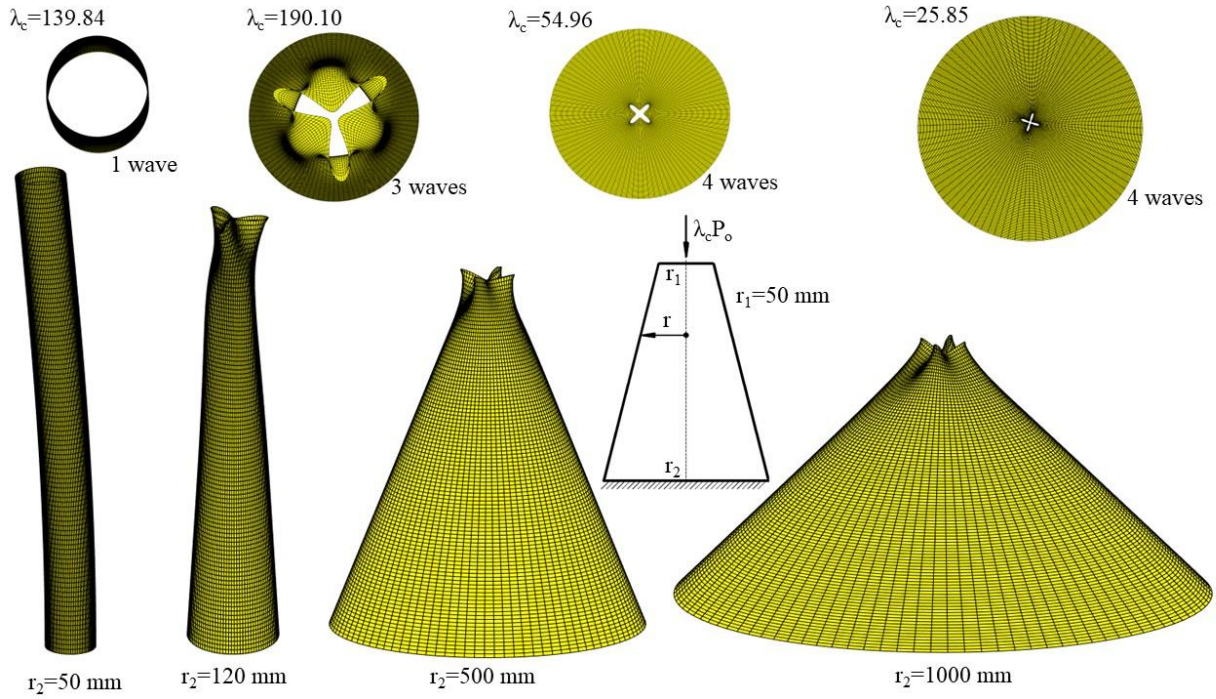

Figure 6: Buckling modes of cantilever members, obtained with the proposed GBT formulation

Table 1: GBT results vs. SFEA results for buckling of shells under axial compression

r_2 [mm]	λ_c GBT	Difference GBT vs SFEA (%)	Modes *k, i , j*
50	139.84	0.01	3
60	204.64	0.64	3
70	220.36	0.71	5
90	214.65	0.08	5
100	212.76	0.20	5
120	190.10	0.05	7
150	162.12	0.21	9
200	128.60	0.38	9
300	89.83	0.19	9
400	68.33	0.43	9
500	54.96	0.47	9
1000	25.85	0.70	9

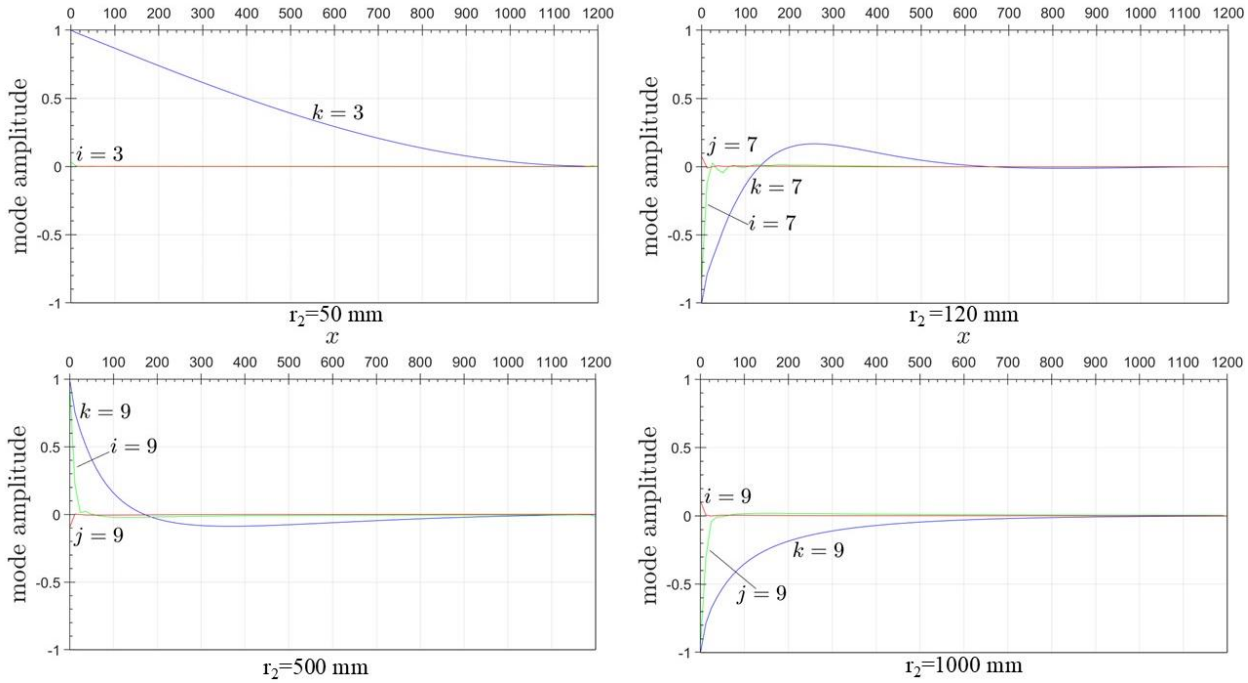

Figure 7: Mode amplitudes for the buckling modes of four shells under axial compression

5. Conclusions

This paper presented the first GBT formulation for the geometrically non-linear analysis of thin truncated conical shells with circular cross-sections, undergoing complex cross-section deformation. Compared with the previous GBT formulations (available for the linear and linearized buckling analyses cases only), this study considers all the membrane strain components in the kinematic relations and is able to perform first-order, linearized buckling and second-order analyses. Even though the formulation is necessarily complex, due to the intricate kinematics of conical shells, all expressions required to implement a suitable displacement-based finite element were provided in a straightforward vector-matrix format. The examples provided in the paper provide solid evidence that the formulation is extremely accurate for linear and linearized stability analyses, while it is quite accurate up to fairly large displacements. Moreover, the GBT modal solution is capable of providing insightful information, while the analyses generally trigger a relatively small number of deformation modes and require only a few finite elements.

This proposal lays the groundwork for more extensive research into the structural behavior of conical shells, especially when it comes to stability and vibration. Work is under way to cover not only these aspects, but also to allow tracing complex equilibrium paths, include imperfections and calculate true collapse loads involving elastoplastic material behavior.

References

Bathe, K. J. (2019), ADINA System, ADINA R&D Inc.

Goldfeld, Y. (2007), Imperfection sensitivity of laminated conical shells, *Solids and Structures*, 44, 1221–1241.

Gonçalves, R., Camotim, D. (2013). "On the behaviour of thin-walled steel regular polygonal tubular members." *Thin-Walled Structures*, 62 191–205.

Gonçalves, R., Nedelcu, M. (2024). "First-order GBT for truncated conical shells with circular cross-section." *Thin-Walled Structures*, 203 112210.

Hibbit, Karlsson and Sorensen Inc. (2002). *ABAQUS Standard* (Version 6.14-1).

Leissa, A. (1973). *Vibration of shells*, Vol. 288, Scientific and Technical Information Office, National Aeronautics and Space Administration.
Mureşan, A.-A., Nedelcu, M., R. Gonçalves, R. (2019). "GBT-based FE formulation to analyse the buckling behaviour of isotropic conical shells with circular cross-section." *Thin-Walled Structures*, 134 84–101.
Nedelcu, M. (2011). "GBT formulation to analyse the buckling behaviour of isotropic conical shells." *Thin-Walled Structures*, 49 (7) 812–818.
Schardt, R. (1989). *Verallgemeinerte Technische Biegetheorie*, Berlin, Springer Verlag.
The MathWorks Inc., (2024), *MATLAB version 24.2.0.2740171* (R2024b) Update 1, Massachusetts.